Communication

Ternary Ag/Ag$_3$PO$_4$/MIL-125-NH$_2$ Z-scheme heterojunction for boosted photocatalytic Cr(VI) cleanup under visible light

Yun-Cai Zhou, Peng Wang, Huifen Fu, Chen Zhao, Chong-Chen Wang*

Beijing Key Laboratory of Functional Materials for Building Structure and Environment Remediation, Beijing University of Civil Engineering and Architecture, Beijing 100044, China

ABSTRACT

The binary Ag$_3$PO$_4$/MIL-125-NH$_2$ (AMN-X) composites were synthesized through ion exchange-solution method, and the ternary Ag/Ag$_3$PO$_4$/MIL-125-NH$_2$ (AAMN-X) Z-scheme heterojunctions were prepared *via* the photo chemical reduction deposition strategy. The photocatalytic hexavalent chromium (Cr(VI)) sequestration over AMN-X and AAMN-X were investigated under visible light. AAMN-120 accomplished superior reduction performance due to that Ag nanoparticles (NPs) act as electrons transfer bridge to enhance the separation efficiency of photogenerated e$^-$-h$^+$ pairs, in which the reaction rates (k value) were 2.77 and 124.2 fold higher than those of individual MIL-125-NH$_2$ and Ag$_3$PO$_4$, respectively. The influences of different pH values, small organic acids and coexisting ions on the photocatalytic performance of AAMN-120 were also investigated. In addition, the AAMN-120 heterojunction expressed great reusability and stability in cycling experiments. The mechanism of photocatalytic Cr(VI) was investigated and verified through photoluminescence (PL), electrochemistry, electron spin resonance (ESR), active species capture, and Pt element deposition experiments.

© 2020 Chinese Chemical Society and Institute of Materia Medica, Chinese Academy of Medical Sciences. Published by Elsevier B.V. All rights reserved.

Just recently, metal organic frameworks (MOFs) have attracted increasing attention as potential photocatalysts [1,2]. For the photocatalytic activity of MOFs, many researches focused on the application of CO$_2$ reduction, water decomposition, organic pollutant degradation and Cr(VI) reduction due to its outstanding characteristics of large specific surface area, adjustable pore size and good topological structure [1–4]. The construction of heterojunctions between MOFs and semiconductors is increasingly used to improve their photocatalytic activity under visible light or even sunlight. Lately, some silver based semiconductors are considered to be promising visible responsive photocatalysts. Among them, Ag/Ag$_3$PO$_4$ is considered as a highly efficient co-existence photocatalyst, in which Ag particles can not only produce surface plasmon resonance (SPR) effect or electron mediator to boost the absorption of visible light, but also avoid retard the light corrosion of Ag$_3$PO$_4$ [5]. Cui *et al.* constructed Ag/Ag$_3$PO$_4$/RGO heterojunction to improve the performance of photocatalytic organic contaminants degradation [6]. Majid *et al.* reported that the construction of HKUST-1@Ag/Ag$_3$PO$_4$ can enhance the performance of Ponceau BS degradation

under visible light [7]. Cr(VI), as a typical heavy metal, is a common pollutant discharged from textile manufacturing, steel manufacturing, leather tanning, and other industrial fields [8]. The photocatalytic reduction of Cr(VI) to Cr(III) is considered as a feasible strategy to reduce its toxicity and easily eliminate it from environment [9,10].

Herein, MIL-125-NH$_2$ was selected to combine Ag/Ag$_3$PO$_4$ to construct Ag/Ag$_3$PO$_4$/MIL-125-NH$_2$ composites for effective Cr(VI) reduction under visible light. In addition, the stability and mechanism of Ag/Ag$_3$PO$_4$/MIL-125-NH$_2$ Z-scheme heterojunction were also discussed.

The disk-like MIL-125-NH$_2$ was solvothermally synthesized according to a previous report with slight modification (Supporting information) [11]. The binary Ag$_3$PO$_4$/MIL-125-NH$_2$ (AMN-X, like AMN-40, 100, 120, 150) were prepared through ion-exchange-solution method (Supporting information). The ternary Ag/Ag$_3$PO$_4$/MIL-125-NH$_2$ (AAMN-X, like AAMN-40, 100, 120, 150) were fabricated *via* photo chemical reduction deposition approach (Fig. 1a). Taking AAMN-120 for an example, the obtained AMN-120 composite was added to 100 mL distilled water, and the suspension was ultrasonicated for 10 min. The system was then illuminated using a 500 W Xe light (Beijing Aulight Co., Ltd.) for 60 min to reduce partial Ag$^+$ ions on the surface of AMN-120 into Ag^0 element. Finally, the powder was collected by filtration, cleaned

---

* Corresponding author.
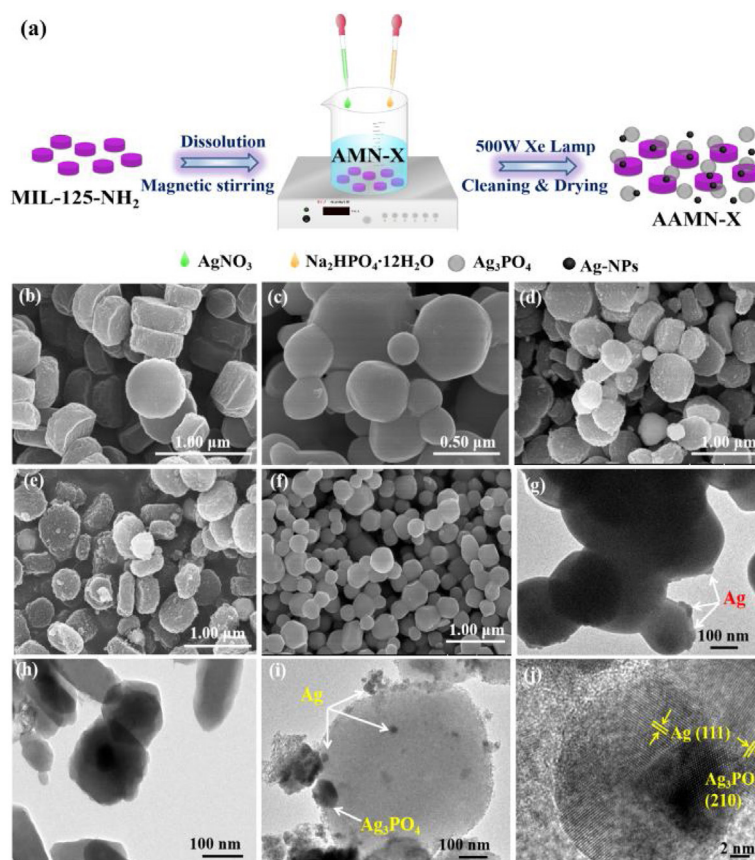*E-mail address:* wangchongchen@bucea.edu.cn (C.-C. Wang).

Fig. 1. (a) Schematic formation of the AAMN-X composites; SEM images of (b) MIL-125-NH$_2$, (c) Ag$_3$PO$_4$, (d) AMN-120, (e) AAMN-120 and (f) Ag/Ag$_3$PO$_4$; TEM images of (g) Ag/Ag$_3$PO$_4$, (h) MIL-125-NH$_2$ and (i) AAMN-120; (j) HRTEM of AAMN-120.

with ultra-pure water for several times, and dried oven at 60 °C overnight. Similarly, other AAMN-X composites with different proportions were prepared following the fabrication procedure of AAMN-120. For the sake of comparison, the Ag/Ag$_3$PO$_4$ nanoparticles was prepared according to the identical method of AAMN-120 fabrication method without adding MIL-125-NH$_2$.

The scanning electron microscope (SEM) (Figs. 1b–e) and transmission electron microscope (TEM) image of MIL-125-NH$_2$ (Fig. 1h) revealed that the sphere-like structure Ag$_3$PO$_4$ were uniformly dispersed on the disk-like MIL-125-NH$_2$. The Ag/Ag$_3$PO$_4$ maintained the morphology of the pristine Ag$_3$PO$_4$ (Fig. 1f), in which the minor Ag^0 nanoparticles (NPs) were distributed over the surface of Ag$_3$PO$_4$ (TEM as illustrated in Fig. 1g). The formation of Ag/Ag$_3$PO$_4$/MIL-125-NH$_2$ (like AAMN-120) was further affirmed by both TEM and high resolution TEM (HRTEM) (Figs. 1i and j), in which the lattice fringe of 0.236 nm and 0.266 nm observed in HRTEM corresponded to the (111) and (210) facets of Ag^0 and Ag$_3$PO$_4$ nanoparticles, respectively [12]. The element mapping results (Fig. S3 in Supporting information) of AAMN-120 revealed the uniform distribution of Ag, O, P, Ti, N, and C elements, further confirming the successful construction of Ag/Ag$_3$PO$_4$/MIL-125-NH$_2$.

The AAMN-X were further characterized by powder X-ray diffraction (PXRD) and Fourier transform infrared (FTIR) (Figs. S4a and S4b in Supporting information). The PXRD peaks of MIL-125-NH$_2$ were in good agreement with those reported in the former literature [13]. The simulated XRD pattern of Ag$_3$PO$_4$ and the

standard pattern of cubic Ag$_3$PO$_4$ matched well, indicating that Ag$_3$PO$_4$ has been successfully prepared (JCPDS No. 97-000-1530) (Fig. S5 in Supporting information). The Ag/Ag$_3$PO$_4$ depicted the identical PXRD patterns to the pure Ag$_3$PO$_4$, suggesting that the incorporation of Ag particles exerted minor effect on the phase structure and crystallite size of Ag$_3$PO$_4$. The characteristic peaks of Ag and Ag$_3$PO$_4$ were observed in the PXRD patterns of AAMN-X particles, and the characteristic peaks of Ag$_3$PO$_4$ were also observed in AMN-X, indicating that AMN-X and AAMN-X were successfully prepared (Figs. S4a and S6 in Supporting information) [14]. AMN-X and AAMN-X displayed typical vibrational bands of carboxylate groups (1400–1700 cm^{-1}) in MIL-125(Ti)-NH$_2$ [15]. The peaks around 1040 and 550 cm^{-1} were related to the asymmetric stretching vibration modes of P—O—P and bending vibration of O=P—O of Ag$_3$PO$_4$ [16]. In their UV–vis diffuse reflection spectra (UV–vis DRS), the absorption edges of MIL-125-NH$_2$ and Ag$_3$PO$_4$ were determined as *ca.* 465 and 532 nm with the E_g as *ca.* 2.67 and 2.33 eV, respectively (Figs. S4c and S4d in Supporting information). The energy gap of AAMN-120 (E_g = 2.55 eV) was smaller than that of AMN-120 (E_g = 2.71 eV) owing to the surface plasmon absorption effect of Ag^0 (Fig. S4d), also indicating that the AAMN-120 composite can be excited by visible light [17].

X-ray photoelectron spectroscopy (XPS) (Fig. S7 in Supporting information) was used to further verify the surface composition and chemical state of AAMN-120. The typical peaks of elements in both Ag$_3$PO$_4$ and MIL-125-NH$_2$ were presented simultaneously in

the spectrum of AAMN-120 (Fig. S7a). The Ag 3d, Ti 2p, P 2p, C 1s, N 1s, and O 1s spectrum of AAMN-120 were analyzed detailly in Supporting information. The spectrum of Ag 3d in Ag/Ag_3PO_4 (Fig. S8 in Supporting information) can be delimited to two parts at about 367.99/374.10 eV and 367.06/371.45 eV, corresponding to Ag^0 and Ag^+, respectively [18,19].

The photocatalytic Cr(VI) decontamination activities of different photocatalysts upon the illumination of visible light were explored at pH 2.0, as shown in Figs. 2 a and b. It was found that the increase of MIL-125-NH_2 content in binary AMN-40, AMN-100 and AMN-120 as well as ternary AAMN-40, AAMN-100, and AAMN-120 resulted in increasing photocatalytic efficiencies (Fig. 2a) and improved reaction rates (k value) fitted by *pseudo*-first-order-kinetic model (Fig. 2b). It was worth noting that AAMN-X possessed superior photocatalytic activities to AMN-X, probably due to that the existence of Ag NPs could promote the separation of photogenerated electrons and holes. As demonstrated in Fig. 2b, the reaction rate (k value) of AAMN-120 was 0.0621 min^{-1}, 1.73, 2.77 and 124.2 times higher than those of AMN-120, MIL-125-NH_2 and Ag_3PO_4, respectively. However, the excessive introduction of MIL-125-NH_2 into AMN-X (like AMN-150) and AAMN-X (AAMN-150) inhibited their photocatalytic efficiencies, which was assigned to the declined separation of photogenerated electrons and hole pairs [20]. The BET specific surface area (SSA) of Ag/Ag_3PO_4 is determined as 12.1 m^2/g. While, the BET SSA of AAMN-120 is measured as 478.95 m^2/g (Fig. S9 in Supporting information) due to the large SSA up to 1000 m^2/g of MIL-125-NH_2 [15,21]. The higher specific surface area of AAMN-120 can provide

enough active sites to enhance the photocatalytic performance. Therefore, AAMN-120 was selected as the most suitable photocatalyst for the successive experiments.

To determine the apparent quantum efficiency (AQE) during the Cr(VI) reduction, several optical filters (FWHM = 15 nm) were adopted to yield incident light with different wavelengths (Fig. 2c, Table S1 in Supporting information). The results revealed that the AQE curve was consistent with the UV–vis DRS plot, clarifying that the Cr(VI) reduction was driven by photo-induced process.

As illustrated in Fig. 2d, the highest photocatalytic Cr(VI) sequestration efficiency of occurred at pH 2.0 (91.0% in 50 min and 100.0% in 70 min) (Table S2 in Supporting information). Under acid condition, sufficient H^+ can promote the transformation of Cr(VI) to Cr(III) (following Eqs. (1 and 2) [8]). With the increase of pH, the zeta potential (Fig. S10 in Supporting information) of AAMN-120 became more negative, which could electronically repel with $Cr_2O_7^{2-}$ and CrO_4^{2-}. As the pH further increased to *ca.* 6.0, the Cr(VI) sequestration followed Eq. 3 [20], in which the formed Cr$(OH)_3$ precipitates on the surface of AAMN-120 will cover the active sites to inhibit the photocatalytic efficiency.

$$AAMN\text{-}X\ (AMN\text{-}X) + h\nu \rightarrow AAMN\text{-}X\ (AMN\text{-}X)\ (h^+ + e^-) \quad (1)$$

$$Cr_2O_7^{2-} + 14H^+ + 6e^- \rightarrow 2Cr^{3+} + 7H_2O \quad (2)$$

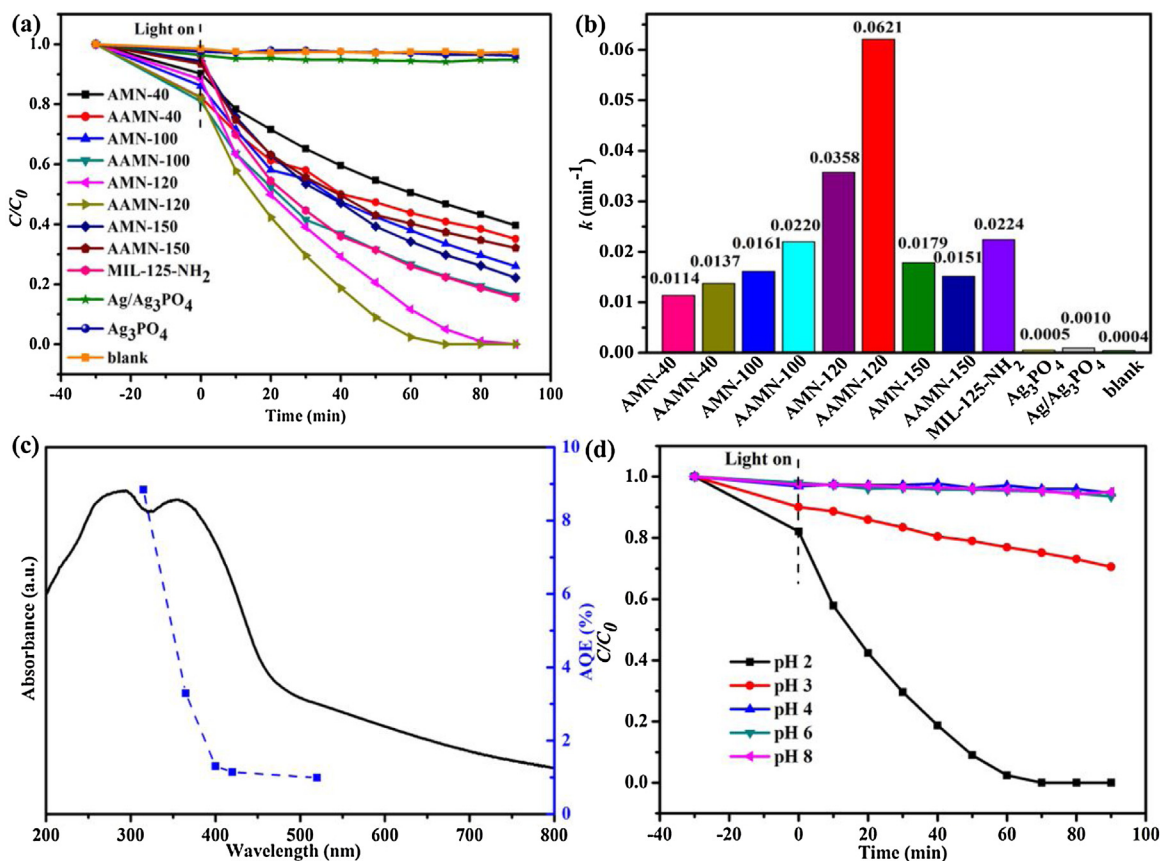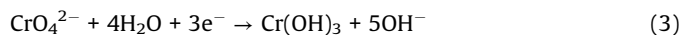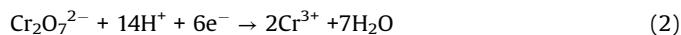$$CrO_4^{2-} + 4H_2O + 3e^- \rightarrow Cr(OH)_3 + 5OH^- \quad (3)$$

Fig. 2. (a) The adsorption and photocatalytic performance and (b) the photocatalytic reduction rates (k values) of samples prepared toward Cr(VI); (c) AQE of Cr(VI) reduction over AAMN-120 at various monochromatic light; (d) Photocatalytic Cr(VI) reduction efficiencies at different pH values over AAMN-120. Reaction condition: initial Cr(VI) concentration is 10 mg/L, the AAMN-120 dosage is 20 mg, volume is 80 mL, pH 2.0.
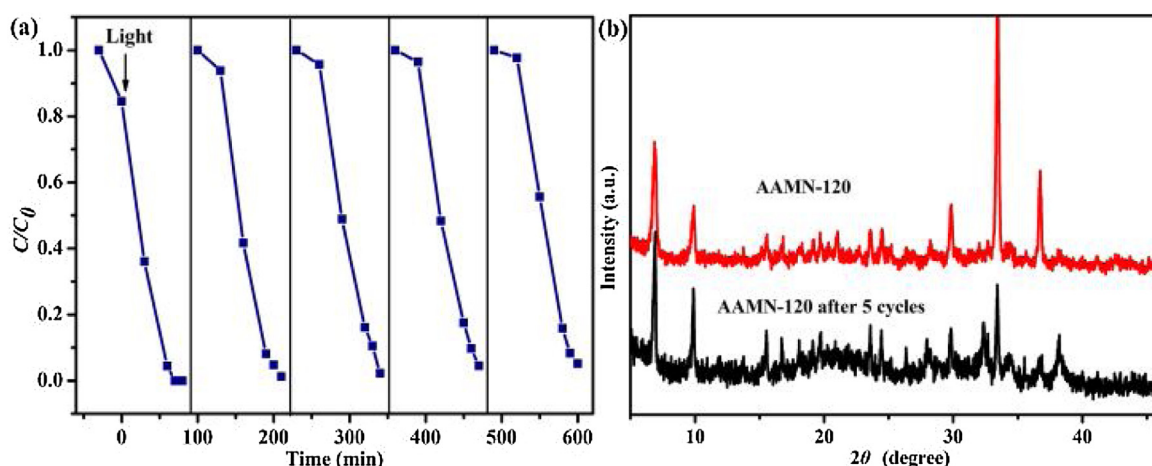
Fig. 3. (a) The reusability of AAMN-120 toward Cr(VI) under visible light. (b) Comparison of PXRD before and after five cycles of photocatalytic Cr(VI) over AAMN-120.

To check the influence of different hole scavengers toward photocatalytic Cr(VI) sequestration, tartaric acid, oxalic acid and citric acid were introduced into the Cr(VI) reduction reaction system (pH 2.0). The photocatalytic reaction rates before 50 min followed the order of tartaric acid > citric acid > oxalic acid (Fig. S11a in Supporting information), which is consistent with the number of α-hydroxyl carboxylate groups in small organic acids [22]. Organic matter in lake water can consume holes and accelerate the separation of electrons holes pairs, thus accelerating Cr(VI) sequestration (Fig. S11b in Supporting information). It was worth noting that inorganic ions in tap water (Table S3 in Supporting information) exerted no obvious inhibition on the Cr(VI) sequestration ability.

The active species capture experiment can provide some solid information to understand the intrinsic reaction of photocatalytic Cr(VI) sequestration (Fig. S11c in Supporting information). The addition of EDTA-2Na enhanced the photocatalytic Cr(VI) reduction activity as it can capture the formed holes. The Cr(VI) sequestration efficiency was greatly suppressed by pumping N_2 into the reaction system because the introduction of N_2 gas can inhibit the formation of $O_2^{\bullet-}$ radicals. It was believed that both $O_2^{\bullet-}$ and photo-induced e^- controlled the Cr(VI) reduction process. The electron spin resonance (ESR) measurements results further confirmed that $O_2^{\bullet-}$ radicals were produced in the photocatalytic process (Fig. S11d in Supporting information).

The recyclability and stability of the AAMN-120 photocatalyst was also investigated (Fig. 3a). After five cycles, AAMN-120 maintained excellent photocatalytic activity, and there was no change in PXRD (Fig. 3b), FTIR spectra (Fig. S12a in Supporting information) and SEM (Fig. S12b in Supporting information). And the XPS after photocatalytic reaction further confirmed the integrity of the surface chemical state of AAMN-120 (Fig. S13 in Supporting information). Further and detailed analyse of PXRD, FTIR, SEM, XPS spectra were listed in Supporting information. Being compared with the counterpart photocatalysts, the photocatalytic activity of AAMN-120 is higher for Cr(VI) reduction under the identical reaction conditions (Table S4 in Supporting information).

The lower PL peak of AAMN-120 (Fig. S14a in Supporting information) informed us that the recombination of photogenerated e^- and h^+ was effectively inhibited [23], which was confirmed by the transient current response results (Fig. S15 in Supporting

information). The EIS (Fig. S14b in Supporting information) clearly expressed that AAMN-120 had the smallest Nyquist radius, suggesting that the highest charges separation rate and the fastest charge transfer was achieved in AAMN-120 [24].

The E_{FB} of MIL-125-NH$_2$ was measured to be *ca.* -0.58 eV *vs.* the Ag/AgCl electrode at pH 2 (Fig. S14c in Supporting information). Therefore, HOMO of MIL-125-NH$_2$ was calculated as 2.29 eV *vs.* NHE at pH 2.0. The valence band (VB) of Ag$_3$PO$_4$ was determined to be 2.53 eV with the aid of XPS measurement (Fig. S14d in Supporting information). Combined with E_g value of Ag$_3$PO$_4$, the conduction band (CB) of Ag$_3$PO$_4$ should be 0.2 eV, which is consistent with that in other literatures [7,16,25]. In order to further determine the transfer path of photogenerated electrons, the photo-deposition of Pt was conducted over AAMN-120.

It can be seen from Figs. 4a and b that Ag NPs not only cover MIL-125-NH$_2$ and Ag$_3$PO$_4$, but also exist at their junction, which provides an efficient medium for the possible charge transfer between them. It can be observed that the Pt element after photo-deposition mainly adhere to the MIL-125-NH$_2$, indicating that there were abundant electrons aggregation on the MIL-125-NH$_2$ [19,26].

On the basis of the above discussion and analyses, the possible Z-scheme mechanism of Cr(VI) cleanup was proposed (Fig. 4c). When the AAMN-120 composite was irradiated by visible light, both MIL-125-NH$_2$ and Ag$_3$PO$_4$ can be excited to produce photogenerated electrons and holes. The photo-induced e^- over CB of Ag$_3$PO$_4$ could easily migrate to Ag^0 NPs (electrons transfer I: Ag$_3$PO$_4$ CB → Ag^0) through the Schottky barrier owing to that the CB potential of Ag$_3$PO$_4$ was more negative than the Fermi level of metal Ag^0 (2.3 eV) [27]. The Fermi level of Ag^0 NPs was more positive than the HOMO of MIL-125-NH$_2$. Therefore, the holes accumulated over the HOMO of MIL-125-NH$_2$ could also easily flow to Ag^0 NPs (electrons transfer II: Ag^0 → MIL-125-NH$_2$ HOMO), which was faster than the recombination of the charge carriers over the HOMO and LUMO of MIL-125-NH$_2$ [17]. Finally, the Z-scheme electron transfer occurs in the Ag/Ag$_3$PO$_4$/MIL-125-NH$_2$ systems, in which Ag^0 NPs act as the electrons transfer medium to promote the separation of photo-induced charge carriers. The photo-induced electrons over MIL-125-NH$_2$ can directly involve in the reduction of Cr(VI), which was consistent with the experimental results of introducing nitrogen into the system (Fig. S11c). Meanwhile, the e^- on the LUMO of MIL-125-NH$_2$ were
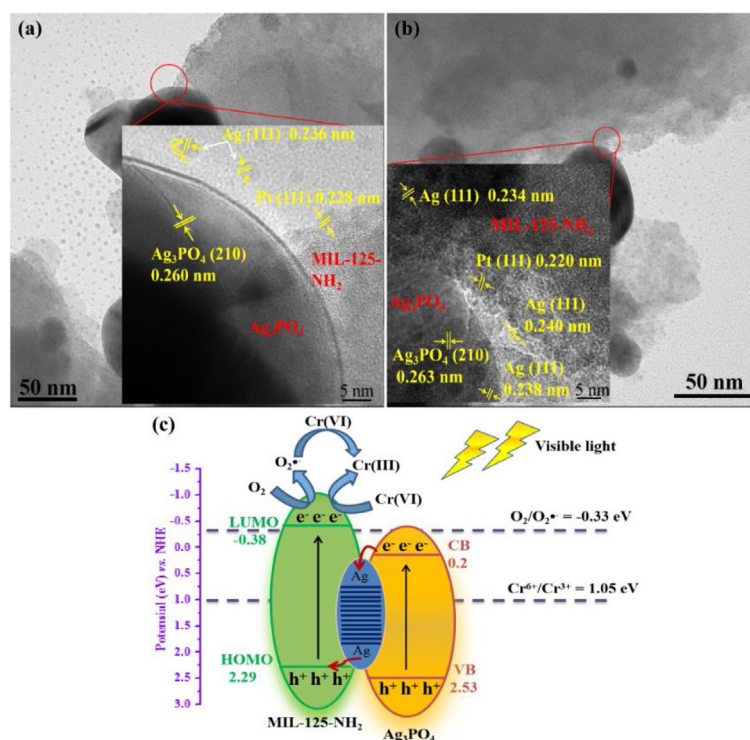
Fig. 4. (a) and (b) TEM image of Pt-loaded AAMN-120 (inserted figure is HRTEM of corresponding TEM area). (c) Schematic illustration and the proposed mechanism of photocatalytic Cr(VI) cleanup over AAMN-120 under visible light irradiation.

captured by O_2 continuously to form $O_2^{\bullet-}$ to further reduce Cr(VI) ($E(O_2/O_2^{\bullet-})$ = –0.33 eV vs. NHE). Therefore, the effective transfer of photogenerated carriers in the Z-Scheme $Ag/Ag_3PO_4/$ MIL-125-NH$_2$ heterojunction led to the enhanced photocatalytic Cr(VI) cleanup.

In summary, we have developed a highly efficient and stable photocatalyst (AAMN-X) for the reduction of hexavalent chromium under visible light, in which AAMN-120 composite possessed excellent properties toward Cr(VI) sequestration at pH 2.0. It was found that some small organic acids and dissolved organic matters in lake water can accelerate the reduction of Cr (VI), while the inorganic ions in tap water can inhibit the photocatalytic ability. The improvement of photocatalytic activity was assigned to the enhancement of photogenerated electrons and holes transfer with the aid of the Z-scheme heterojunction. The ESR, active species capture experiments, and Pt deposition experiments proved that both $O_2^{\bullet-}$ and photogenerated e$^-$ controlled the Cr(VI) reduction. It was an effective and controllable strategy to prepare the Ag^0/Ag-based semiconductors composites via the in-situ self-sacrifice reaction of Ag$^+$ into Ag^0 upon the irradiation of visible light, which can be used to modify some metal-organic frameworks (MOFs) to accomplish boosted photocatalytic performance for environment remediation and ecological sustainability.

Declaration of competing interest

The authors declare that they have no known competing financial interests or personal relationships that could have appeared to influence the work reported in this paper.

Appendix A. Supplementary data

Supplementary material related to this article can be found, in the online version, at doi:https://doi.org/10.1016/j.cclet.2020.02.048.

References

[1] C.C. Wang, X.D. Du, J. Li, et al., Appl. Catal. B: Environ. 193 (2016) 198–216.
[2] T. Zhang, W. Lin, Chem. Soc. Rev. 43 (2014) 5982–5993.
[3] R.J. Kuppler, D.J. Timmons, Q.R. Fang, et al., Coord. Chem. Rev. 253 (2009) 3042–3066.
[4] Y.X. Li, H. Fu, P. Wang, et al., Environ. Pollut. 256 (2020) 113417.
[5] P. Zhou, J. Yu, M. Jaroniec, Adv. Mater. 26 (2014) 4920–4935.
[6] C. Cui, Y. Wang, D. Liang, et al., Appl. Catal. B: Environ. 158-159 (2014) 150–160.
[7] F.A. Sofi, K. Majid, O. Mehraj, J. Alloys. Compd. 737 (2018) 798–808.
[8] X.H. Yi, S.Q. Ma, X.D. Du, et al., Chem. Eng. J. 375 (2019) 121944.
[9] D.D. Chen, X.H. Yi, C. Zhao, et al., Chemosphere 245 (2020) 125659.
[10] X. Wang, W. Liu, H. Fu, et al., Environ. Pollut. 249 (2019) 502–511.
[11] H. Wang, X. Yuan, Y. Wu, et al., J. Hazard. Mater. 286 (2015) 187–194.
[12] S. Nayak, K.M. Parida, ACS Omega 3 (2018) 7324–7343.
[13] D. Sun, W. Liu, Y. Fu, et al., Chem. Eur. J. 20 (2014) 4780–4788.
[14] G. Fan, X. Zheng, J. Luo, et al., Chem. Eng. J. 351 (2018) 782–790.
[15] B. Kim, Y.R. Lee, H.Y. Kim, W.S. Ahn, Polyhedron 154 (2018) 343–349.
[16] J. Lu, Y. Wang, F. Liu, L. Zhang, S. Chai, Appl. Surf. Sci. 393 (2017) 180–190.
[17] L. Ye, J. Liu, C. Gong, et al., ACS Catal. 2 (2012) 1677–1683.
[18] J. Qiu, M. Li, H. Wang, J. Yao, Chemosphere 242 (2020) 125197.
[19] W. Zhao, T. Ding, Y. Wang, et al., Chin. J. Catal. 40 (2019) 1187–1197.
[20] Y.C. Zhou, X.Y. Xu, P. Wang, et al., Chin. J. Catal. 40 (2019) 1912–1923.
[21] S.N. Kim, J. Kim, H.Y. Kim, H.Y. Cho, W.S. Ahn, Catal. Today 204 (2013) 85–93.

[22] X.H. Yi, F.X. Wang, X.D. Du, P. Wang, C.C. Wang, Appl. Organomet. Chem. 33 (2019) e4621.
[23] J. Chen, J. Zhan, Y. Zhang, Y. Tang, Chin. Chem. Lett. 30 (2019) 735–738.
[24] Z. Cai, X. Hao, X. Sun, et al., Water Res. 162 (2019) 369–382.
[25] F.A. Sofi, K. Majid, Mater. Chem. Front. 2 (2018) 942–951.
[26] W. Jiang, X. Zong, L. An, et al., ACS Catal. 8 (2018) 2209–2217.
[27] C. Liang, C.G. Niu, H. Guo, et al., Catal. Sci. Technol. 8 (2018) 1161–1175.